NeuroImage 195 (2019) 362–372

Contents lists available at ScienceDirect

NeuroImage

journal homepage: www.elsevier.com/locate/neuroimage

Multi-site repeatability and reproducibility of MR fingerprinting of the healthy brain at 1.5 and 3.0 T☆

Guido Buonincontri [a,b], Laura Biagi [a,b], Alessandra Retico [c], Paolo Cecchi [d], Mirco Cosottini [d], Ferdia A. Gallagher [e], Pedro A. Gómez [f], Martin J. Graves [e], Mary A. McLean [g], Frank Riemer [e], Rolf F. Schulte [h], Michela Tosetti [a,b,*], Fulvio Zaccagna [e], Joshua D. Kaggie [e]

[a] IMAGO7 Foundation, Pisa, Italy
[b] IRCCS Fondazione Stella Maris, Pisa, Italy
[c] National Institute for Nuclear Physics, Pisa, Italy
[d] Department of Radiology, University of Pisa, Italy
[e] Department of Radiology, University of Cambridge, United Kingdom
[f] Munich School of Bioengineering, Technical University of Munich, Germany
[g] Cancer Research UK Cambridge Institute, University of Cambridge, United Kingdom
[h] GE Healthcare, Munich, Germany

ARTICLE INFO

Keywords:
MRI
Quantitation
Relaxometry
Brain
MR fingerprinting

ABSTRACT

Fully-quantitative MR imaging methods are useful for longitudinal characterization of disease and assessment of treatment efficacy. However, current quantitative MRI protocols have not been widely adopted in the clinic, mostly due to lengthy scan times. Magnetic Resonance Fingerprinting (MRF) is a new technique that can reconstruct multiple parametric maps from a single fast acquisition in the transient state of the MR signal. Due to the relative novelty of this technique, the repeatability and reproducibility of quantitative measurements obtained using MRF has not been extensively studied. Our study acquired test/retest data from the brains of nine healthy volunteers, each scanned on five MRI systems (two at 3.0 T and three at 1.5 T, all from a single vendor) located at two different centers. The pulse sequence and reconstruction algorithm were the same for all acquisitions. After registration of the MRF-derived M_0, T_1 and T_2 maps to an anatomical atlas, coefficients-of-variation (CVs) were computed to assess test/retest repeatability and inter-site reproducibility in each voxel, while a General Linear Model (GLM) was used to determine the voxel-wise variability between all confounders, which included test/retest, subject, field strength and site. Our analysis demonstrated an excellent repeatability (CVs of 2–3% for T_1, 5–8% for T_2, 3% for normalized-M_0) and a good reproducibility (CVs of 3–8% for T_1, 8–14% for T_2, 5% for normalized-M_0) in grey and white matter.

1. Introduction

Among medical imaging modalities, magnetic resonance imaging (MRI) stands out for its excellent soft-tissue contrast, anatomical detail and high sensitivity for disease detection. However, as proven by the continuous and vast effort to develop new MRI techniques, limitations and open challenges remain. The primary source of contrast in MRI images are the various relaxation parameters, e.g. T_1 and T_2 relaxation times, associated with the nuclear magnetic resonance (NMR) phenomena upon which MRI is based. Although it is possible to quantify these relaxation parameters (qMRI) they are rarely used in the clinic, and radiological interpretation of images is primarily based upon images that are relaxation time weighted.

Quantitative changes in longitudinal (T_1) and transverse (T_2) relaxation times in discrete brain regions have been described in neurological disorders such as Alzheimer's disease (Bartzokis et al., 2000) (Tang et al., 2018), Parkinson's disease (Vymazal et al., 1999) (Baudrexel et al., 2010), multiple sclerosis (Larsson et al., 1989) (Gracien et al., 2017), and epilepsy (Pitkanen et al., 1996) (Bernhardt et al., 2018); psychiatric diseases such as autism (Friedman et al., 2003) (Hendry et al., 2006) and

☆ These high repeatability and reproducibility results encourage further investigations of MR Fingerprinting for fast, repeatable and reproducible quantification of MRI signals within clinical use.

* Corresponding author. IRCCS Stella Maris and IMAGO7 Foundation and INFN-Pisa Division, Pisa, Italy.
E-mail address: michela.tosetti@fsm.unipi.it (M. Tosetti).

https://doi.org/10.1016/j.neuroimage.2019.03.047
Received 13 September 2018; Received in revised form 8 March 2019; Accepted 20 March 2019
Available online 25 March 2019
1053-8119/

schizophrenia (Williamson and Pelz, 1992), as well as genetic diseases such as cancer (Yankeelov et al., 2011). The clinical adoption of qMRI is mainly limited by the long acquisition times required to quantify each relaxation parameter as well as questions around their accuracy and reliability. More specifically, the main limitations of qMRI methods have been the difficulty in dealing with the high inter-parameter correlations and a high sensitivity to MRI system imperfections (Deoni, 2010).

Today, more than forty years into clinical MRI, effective qMRI methods are still challenging to achieve within short acquisition times such that they can become clinically relevant and routinely used for disease characterization. Quantitative MRI will ideally improve the reliability of determining subtle disease changes, especially when combined with radiomics (Tofts, 2005). The main challenges for quantifying MRI relaxation times come directly from the physical constraints that limit achievable resolutions and image contrasts within clinically acceptable scan times with sufficient signal-to-noise ratios (SNR). In addition to requiring fast acquisitions, the MRI signal must also be repeatable and reproducible. Briefly, repeatability refers to the degree of agreement between experiments repeated at the same location, using the same measurement procedure and equipment, performed under similar conditions, and repeated at separate time points. In contrast, reproducibility refers to the degree of agreement between the results of experiments conducted at different locations and with similar but separate instruments. In MRI, both of these metrics are affected by variability in electromagnetic fields, including radiofrequency transmit power and static magnetic field non-uniformity (Majumdar et al., 1986) (Sung et al., 2013). In recent years, efficient and repeatable quantitative MRI has been studied through new approaches that estimate multiple parameters simultaneously in a single model. These new multi-parametric quantitative methods include, amongst others, Magnetic Resonance Fingerprinting (MRF) (Ma et al., 2013), MAGnetic resonance Image Compilation (MAGIC) (Tanenbaum et al., 2017), Magnetic Resonance Spin TomograPhy in Time-doman (MR-STAT) (Sbrizzi et al., 2018), and 3D Silent data mining (Wiesinger et al., 2018). These new methods are appealing due to their ability to acquire multiple quantitative maps efficiently within a single acquisition. Quantitative maps derived from these data can then be used to synthesize standard image contrasts to assist in disease assessment.

Magnetic Resonance Fingerprinting (MRF) is an imaging technique that efficiently samples the transient state of the MRI signal. These transient signals may be considered as ‘fingerprints’ that can be retrospectively matched to a dictionary of simulated signal patterns (Ma et al., 2013). To achieve such transient signal ‘fingerprints’, scan parameters such as repetition time (TR) and flip angle are varied between each repetition of an MRI acquisition. The measured signal evolution is then used to find the best parameter match within a dictionary (Ma et al., 2013). The MRF dictionary consists of many precomputed values of the signal evolution for a range of parameters including, but not limited to, T_1 and T_2. The relative ease of implementation makes MRF not only interesting theoretically, but feasible using standard acquisition and reconstruction technology. Due to its high efficiency, MRF has particular potential if it can demonstrate accurate and reproducible quantitative maps that can discriminate diseases across longitudinal and multi-site studies. However, for MRF to be validated and adopted clinically, the quantitative parameters extracted must be shown to be robust, with a high repeatability and reproducibility. While published studies have shown MRF methods to have a high repeatability of T_1 and T_2 values using an ISMRM/NIST phantom (Jiang et al., 2017b), *in vivo* multi-site repeatability and reproducibility studies remain important to assess the clinical value of this novel technique (Körzdörfer et al., 2018).

The objective of this study was to assess the repeatability and reproducibility of MRF derived relaxation time measurements in the brain. The study involved acquiring data from both phantoms and normal volunteers using multiple MRI systems at 1.5 T and 3.0 T located in two different centers.

2. Material and methods

2.1. MRF acquisition and reconstruction

Phantom and human MRF data was acquired on MRI scanners with dedicated head/brain coils using five different systems (Table 1): one 1.5 T and one 3.0 T at the first site (site A) and two 1.5 T systems and one 3.0 T at the second site (site B). All systems were from the same vendor (GE Healthcare, Waukesha, WI, USA).

MRF data was obtained using 2D steady-state free precession (SSFP) with a spiral readout trajectory. The flip angles and repetition times were varied for 979 frames per slice and matched the values from Jiang et al. (2015) (Fig. 1a). A spiral trajectory was rotated by the golden-angle for 89 interleaves, which was then repeated 11 times to provide readout data over 979 frames (Fig. 1b). The total Nyquist field-of-view (FOV) = 256 mm, reconstruction matrix = 128×128, sampling bandwidth = $\pm$250 kHz, echo time = 2.2 ms, scan time was 12.8 s/slice. A total of 55 slices per subject and 40 per phantom were obtained at 2 mm slice thickness with the TR/flip angle lists repeated for each slice.

The sequence was limited to a maximum gradient amplitude of 20 mT/m and slew rate of 50 T/m/s. Each interleave was rewound and followed by a spoiler gradient along the slice-select axis achieving 8π dephasing across each 2 mm thick slice. The maximum gradient strength was limited such that all systems would match trajectories, irrespective of individual system gradient performance. We note that the dominant factor affecting the minimum TR was the gradient slew rate at the 1.5 T wide-bore scanner (1.5 T, Site WB).

Dictionaries including T_1 and T_2 relaxation were computed using the extended phase graph formalism. The static magnetic field (B_0) and the transmit radiofrequency field (B_{1+}) non-uniformity was not included in the dictionary. The slice profile was included to improve T_2 accuracy, which is highly-dependent on the formation of stimulated echoes (Buonincontri and Sawiak, 2016). The values of T_1 and T_2 were then estimated through inner-product pattern matching of the dictionaries to the reconstructed time frames. The relative proton density was calculated as described in (Ma et al., 2013).

Before pattern matching, each undersampled spiral frame was reconstructed using a re-gridding algorithm before an inverse Fourier transformation (Jackson et al., 1991). Coil images were then combined into a single image per frame, based on adaptive coil combination on an average of the time frames (Walsh et al., 2000). Following these reconstruction steps, voxel-wise pattern matching determined the highest correlation between the signal evolution and simulated dictionary (Ma et al., 2013).

2.2. Phantom study

Phantom data were acquired for two repeated scans on each system using the ISMRM/NIST phantom (QalibreMD, Boulder, Co), with the phantom removed then replaced between scans. This retest immediately following the test minimized temperature changes that could alter the relaxation times and thus phantom repeatability (Nelson and Tung, 1987). The phantom temperature at site A was 17 ± 2 °C and at site B was 22 ± 2 °C. No temperature correction was performed.

The *in vivo* dictionary range and step size were the same as those published in (Jiang et al., 2015). The *in vivo* T_1 dictionary resolution used

Table 1
Systems and software versions at the centers participating in this study.

Field Strength	Site	System Model	Software Version	# Receiver Coil Channels	Bore Size
1.5 T	A	HDxt	HD16	8	60 cm
3.0 T	A	MR750	DV25	8	60 cm
1.5 T	B	MR450	DV24	12	60 cm
1.5 T	WB	MR450w	DV26	12	70 cm
3.0 T	B	MR750	DV24	12	60 cm

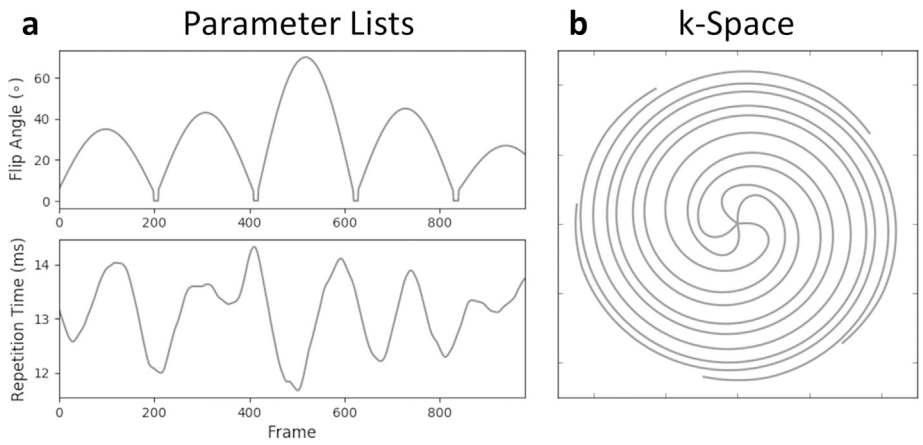

Fig. 1. The (a) parameter lists for the flip angle and repetition time variation and the (b) first five interleaves of the k-space acquisition.

min:step:max values of 20:10:3000,3000:200:5000 ms, and the T_2 dictionary used min:step:max values of 10:5:300,300:50:500 ms. The phantom dictionary was modified for the T_1 and T_2 value range of the vials in the NIST phantom, with higher density at the lower values, with T_1 dictionary values of 10:10:400,400:20:4000 ms, and T_2 dictionary values of 2:1:19,20:2:400,400:50:2000 ms.

Circular regions-of-interest (ROIs) were obtained in the NIST phantom, each ROI consisting of 32 voxels central to each of the 14 vials in either the T_1 or T_2 weighted vial regions, which were used for statistical calculations on the MRF-calculated T_1 and T_2 maps. The coefficient-of-variation (CV) was used both as a measure of repeatability when calculated using the test and retest values, and of reproducibility when calculated using the first measurement (test) at each site (Begley and Ellis, 2012). Bland-Altman plots were created to visualize the agreement between test and retest values (Bland and Altman, 1999).

2.3. Volunteer study

MRF data was acquired from the brains of nine healthy volunteers (2 females, 7 males, ages = 18–55 years). All volunteers underwent imaging at both site locations with 2–6 months between the first and second site imaging (Table 1) with written informed consent in accordance to local ethical approvals of both locations. For each exam, including test and retest sessions, the protocol comprised a localizer, a structural volumetric sequence obtained by using a 1 mm-isotropic T_1-weighted 3D fast spoiled gradient echo (3D BRAVO), and a 2 mm-isotropic multi-slice 2D SSFP MRF (Jiang et al., 2015). Structural images were acquired to enable the registration of the MRF parameter maps to anatomy, and to segment brain tissues (white matter, WM; grey matter, GM; and cerebrospinal fluid, CSF). The subjects were removed and completely re-positioned in each scanner between test and retest sessions.

2.4. In vivo data pre-processing

First, MRF retest images were co-registered to the respective test image. In this step, nearest-neighbor interpolation was used. MRF maps were rigidly co-registered to their respective 3D T_1-weighted images using the Statistical Parametric Mapping (SPM 12) Toolbox (Friston et al., 1994) (Penny et al., 2011). After registration, each subject's volumetric image was warped to match a custom DARTEL atlas based on the subjects studied (Goto et al., 2013). The 3D T_1-weighted volumetric dataset from the 3.0 T at site A was used to estimate the DARTEL template and the transformations to warp brain volumes (including MRF maps) from the subject space to the template space. After applying 6 mm Gaussian smoothing, CVs were calculated between each voxel in test and retest measurements. For each subject, the segmented tissue probability maps were calculated and used to extract mean values of parameters in GM, WM, and CSF. Due to arbitrary receiver gain and scaling, relative M_0 values were reported self-normalized (nM_0) to the average inside the brain mask. A threshold of 50% probability was used as a mask per each tissue class, and a mask containing voxels acquired in all tests was also applied (see Fig. 2). Statistical analysis was conducted using a non-parametric Mann-Whitney *U* test for comparison of the average T_1, T_2 and nM_0 values among subjects obtained at the same magnetic field but with different systems (Mann and Whitney, 1947).

For each measurement (nM_0, T_1 and T_2), scatter plots of test/retest data were generated sampling 1000 random points in each tissue masks and extracting corresponding values for each subject and each system (45000 point total). A linear fit and correlation statistics were performed for each plot. To assess the agreement of the two set of data, Lin's concordance correlation coefficient (Lawrence and Lin, 1989) was calculated for each measurement (nM_0, T_1, T_2) in each tissue (GM, WM, CSF).

2.5. GLM analysis

A General Linear Model (GLM) (Beckmann et al., 2003) was implemented in SPM (Ashburner, 2012) as secondary sensitive method to characterize the effects from several independent physical parameters. GLM analysis was used to describe the maps of physical parameters in terms of a linear combination of explanatory experimental and confounding effects, which was then used to determine residual variability. The covariates modeled as categorical variables were acquisition variability (test/retest data), field strength (1.5 T and 3.0 T), and the acquisition site. The design matrix of our GLM analysis is shown in Fig. 2.

The T_1 and T_2 maps, aligned to the DARTEL template and smoothed, are entered in a multiple linear regression model:

$$Y_i = \beta_0 + \beta_1 X_{i1} + \beta_2 X_{i2} + \beta_3 X_{i3} + \ldots + \beta_p X_{ip} + \varepsilon_i$$

Y_i is the *i*th observation of the dependent variable ($i = 1, \ldots n$, where n is the number of observations). X_{ij} is *i*th observation of the *j*th independent variable ($j = 1, \ldots, p$, where p is the number of independent variables), which represents whether that variable is present in the analysis ($X_{ij} = 1$) or unused ($X_{ij} = 0$). The values β_j represent parameters to be estimated, with β_0 corresponding to the mean value, and ε_i is the variance in the data that cannot be explained by the predictors. The values of the β_j maps quantify the influence of the independent variables on the measured physical parameters T_1 and T_2 at each voxel location. The definition of each β_j in our model is reported in Fig. 2. The estimated effects can be compared by means of voxel-wise statistical analysis. To compare the different effects of variability, we reported the normalized values of β_j averaged over the DARTEL tissue maps, while to take in account possible regional effects of variability, we reported the β_j maps for a representative slice.

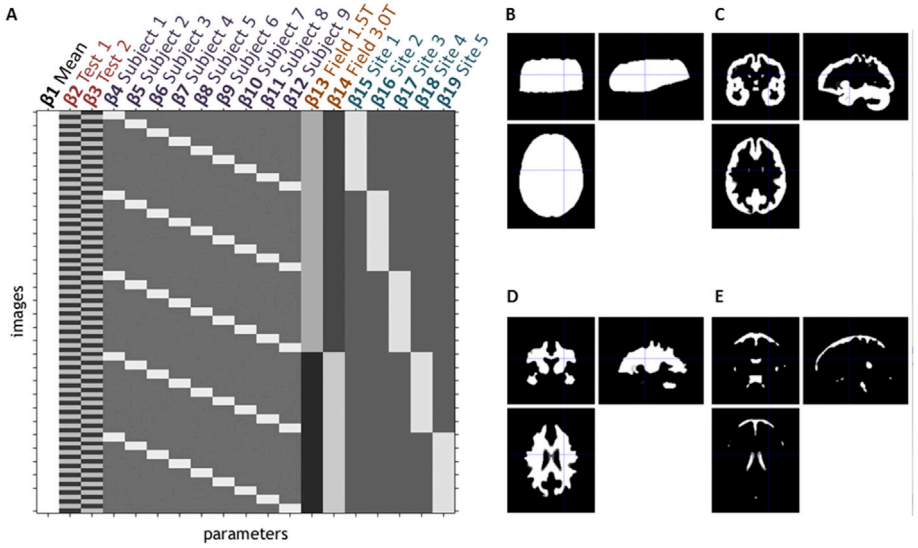

Fig. 2. A) GLM design matrix, B) the TIV mask common to all scanners and subjects, C) grey matter mask, D) white matter mask, E) CSF mask.

2.6. Data and code availability statement

In compliance with funders and institutional ethics approval, the original parametric maps as well as the corresponding structural data for each subject are available at (Kaggie et al., 2019).

3. Results

3.1. Phantom results

Plots from the MRF derived values and NIST phantom values, as

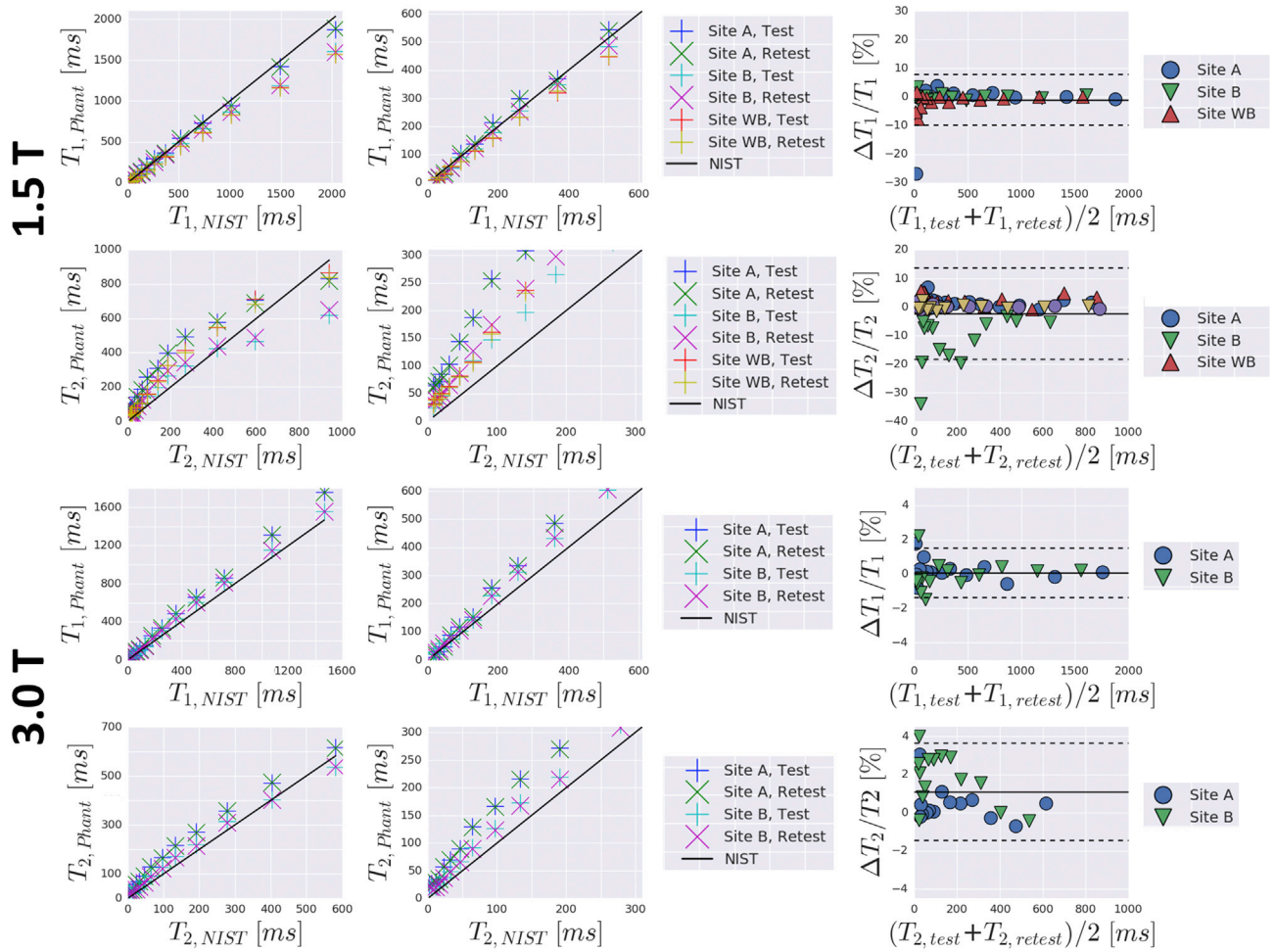

Fig. 3. NIST phantom plots showing the T_1 and T_2 values obtained from MRF against the nominal NIST values at both 1.5 T and 3.0 T (left) and a zoomed view of the plots (middle). The T_1 values demonstrate the highest repeatability, and visually have lower biases (right). The T_2 values show a larger divergence from the nominal NIST values at 1.5 T. Note that the plots extend beyond those previously reported in (Jiang et al., 2017b).

Table 2
Table showing the results of linear regression between the NIST phantom data, as defined in the NIST standard, and from the MRF results.

Field Strength	Site	Param	Slope	Intercept	r-value	p-value
1.5 T	A	T1	0.929	18.816	0.999	<1e-6
1.5 T	B	T1	0.798	24.434	0.999	<1e-6
1.5 T	WB	T1	0.779	14.87	0.999	<1e-6
1.5 T	A	T2	0.891	126.959	0.952	<1e-6
1.5 T	B	T2	0.665	68.100	0.964	<1e-6
1.5 T	WB	T2	0.976	66.064	0.976	<1e-6
3.0 T	A	T1	1.207	10.494	0.999	<1e-6
3.0 T	B	T1	1.068	19.393	0.999	<1e-6
3.0 T	A	T2	1.051	41.578	0.992	<1e-6
3.0 T	B	T2	0.926	25.886	0.995	<1e-6

reported in the NIST guide, are shown in Fig. 3. Linear correlation statistics between the MRF derived values and published NIST values are shown in Table 2. As a measure of repeatability, the intra-site CV phantom values were <1% for all sites and relaxation parameters. As a measure of reproducibility, the inter-site phantom CV values were 0.9% for T_1 and 2.7% for T_2 at 1.5 T, and 0.2% for T_1 and 0.7% for T_2 at 3.0 T. Pearson's correlation and Lin's concordance correlation coefficients (LCCC) for multi-site values of similar phantom vials was greater than 0.99 for both T_1 and T_2 at both field strengths (LCCC = 0.999996 for T_1 at both fields; LCCC = 0.999848 for T_2 at 1.5 T and 0.999967 at 3.0 T).

3.2. Volunteer results

Sample co-registered MRF test and retest images acquired at all centers are shown in Fig. 4. Average values among subjects for T_1, T_2 and nM_0 for each system at each site are reported in Fig. 5.

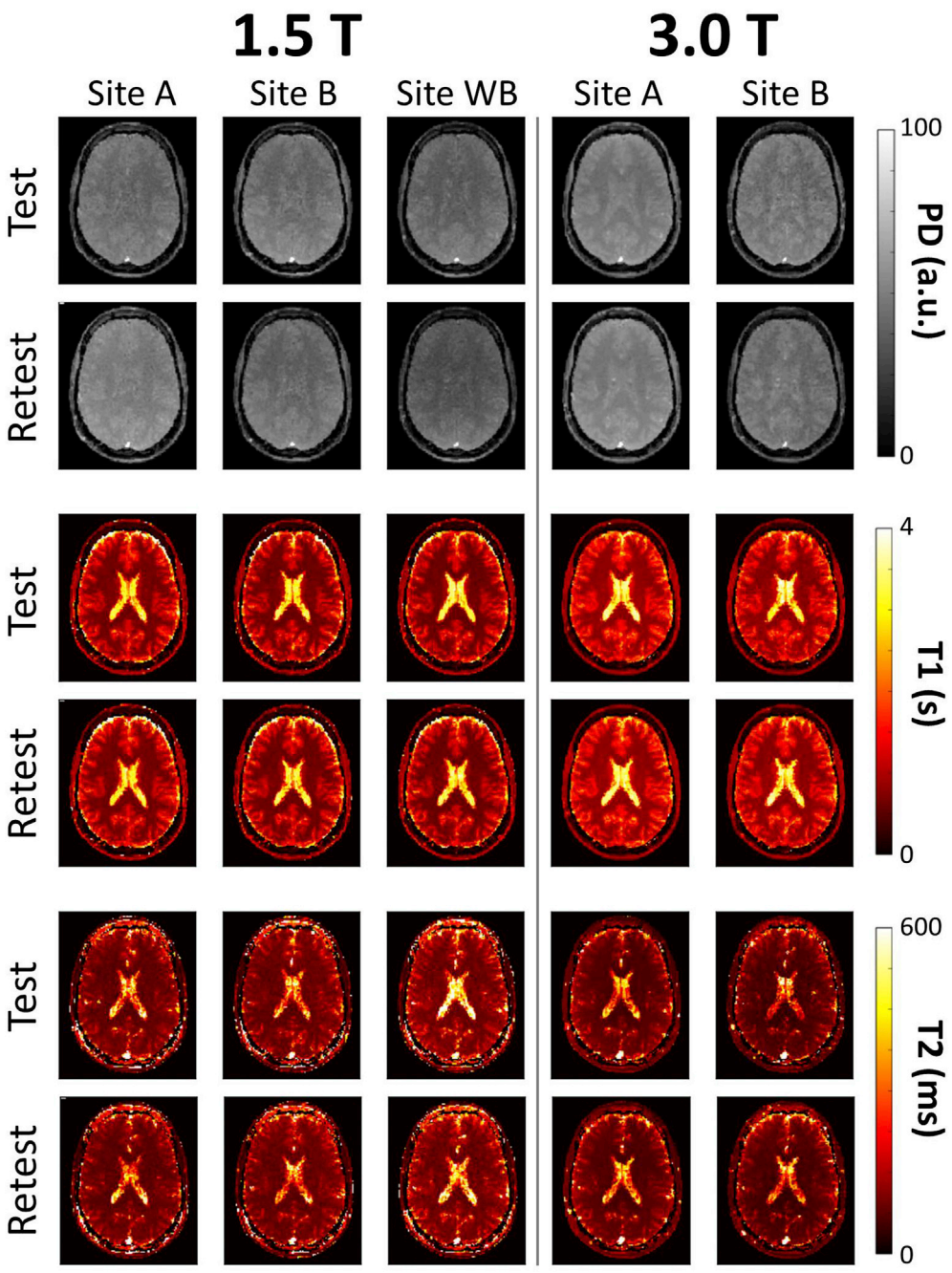

Fig. 4. Images from a single volunteer showing the normalized M0 (proton-density), T1, and T2 maps for a single slice, for both test and retest data at all centers.

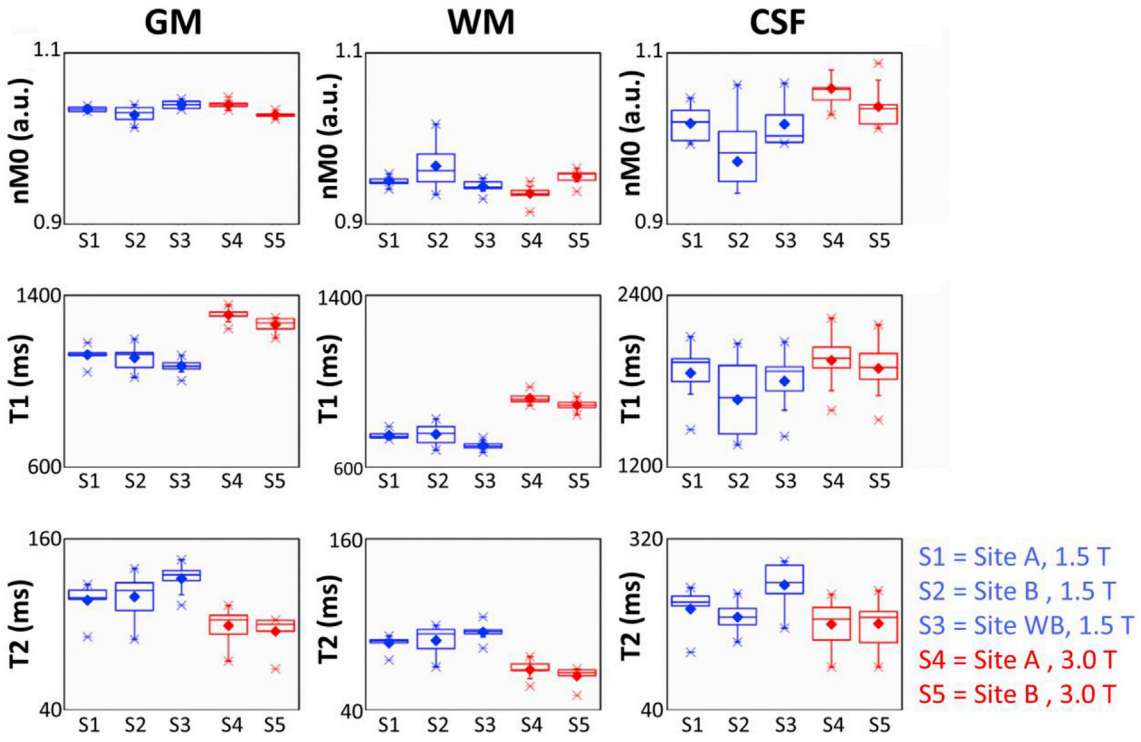

Fig. 5. Mean and standard deviation of T1, T2, and self-normalized M0 (nM0) across grey matter (GM), white matter (WM), and cerebrospinal fluid (CSF). nM0 values greater than 1.0 occur where the defined region has a mean value greater than the normalized value across the entire brain. For each box, whiskers are determined by the minimum and maximum values; diamond indicates the mean value while the line corresponds to the median value.

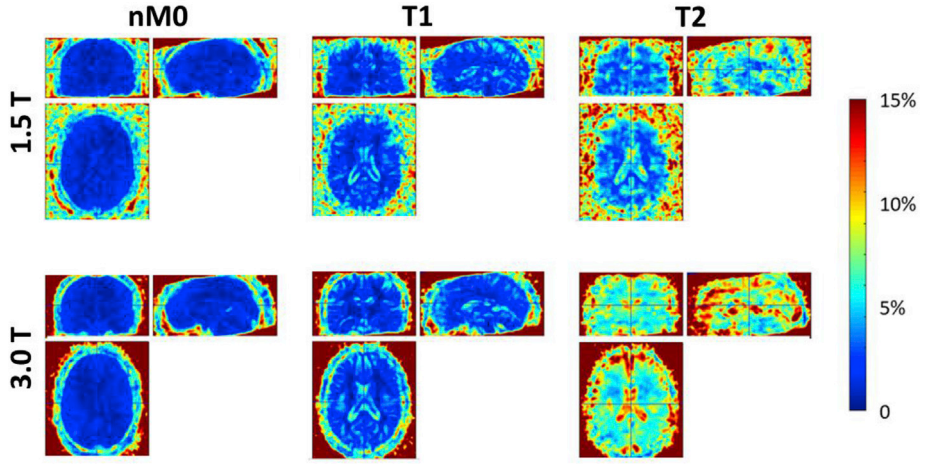

Fig. 6. Group maps of coefficients-of-variation between test and retest at 1.5 T and 3.0 T at site A. Normalized M0 values had the lowest variation, followed by T1, and then T2.

Fig. 6 shows the voxel-wise test/retest performance at 1.5 T and 3.0 T at site A. Normalized M_0 had the lowest variation, which was uniformly under 3% across the brain. Relative T_1 variation was also under 3% at most locations, with some boundary effects at the interface between different tissue classes, possibly due to residual registration errors. Relative T_2 variation was higher at 3.0 T than at 1.5 T, and the CSF regions were the ones showing the highest CV of over 10%.

The results of test/retest CV measurements are reported for each parameter, site and tissue class in Table 3. The T_1-CVs of GM and WM were low (1.9–3.1%, excluding CSF) for all systems, while the T_2-CVs were slightly higher (3.6–7.8%). White matter values (T_1-CVs = 1.9–2.2%; T_2-CVs = 3.6–6.5%) were more repeatable than grey matter values (T_1-CVs = 2.4–3.0%; T_2-CVs = 4.4–7.8%). T_1-CVs demonstrated no field dependency, while the T_2-CVs were lower at 1.5 T (2.9–7.0%) than 3.0 T (4.1–7.8%).

Fig. 7 reports scatter plots and relative linear correlation statistics of test/retest measurements on a voxel-based method. All slopes are about 1 (A = 0.993 to 1.008) and all R^2 indicate strong positive correlations (R^2 = 0.848 to 0.922). According to the classification proposed by McBride (2005), Lin's concordance correlation coefficients reveal a "substantial" agreement of the two dataset for nM_0 (GM/WM/CSF = 0.94/0.95/0.96) and T_1 measurements (0.95/0.96/0.95) and a "moderate" agreement for T_2 (0.92/0.94/0.93). Lin's concordance correlation coefficients results can be assessed on the subject specific plots reported in Supplementary Figures 1 to 9.

The reproducibility results of inter-site group CV measurements are

Table 3
Test/retest coefficients-of-variation (CV) for repeatability of T1, T2, and self-normalized M0 (nM0) across grey matter, white matter, cerebrospinal fluid, and total volume.

T1-CV (%)	Grey matter	White matter	Cerebrospinal fluid	Total Volume
Site A, 1.5 T	2.9	2.1	3.8	2.9
Site B, 1.5 T	3.0	2.1	4.2	3.1
Site WB, 1.5 T	2.4	1.9	3.7	2.6
Site A, 3.0 T	2.7	2.1	3.5	2.8
Site B, 3.0 T	2.7	2.2	3.8	2.8
T2-CV (%)	Grey matter	White matter	Cerebrospinal fluid	Total Volume
Site A, 1.5 T	5.3	3.6	7.9	5.3
Site B, 1.5 T	7.0	4.7	10.5	6.7
Site WB, 1.5 T	4.4	2.9	7.7	4.5
Site A, 3.0 T	7.8	6.5	10.8	7.8
Site B, 3.0 T	6.0	4.1	11.0	6.1
nM0-CV (%)	Grey matter	White matter	Cerebrospinal fluid	Total Volume
Site A, 1.5 T	1.6	1.2	2.2	1.7
Site B, 1.5 T	2.0	1.4	3.0	2.2
Site WB, 1.5 T	1.7	1.3	2.6	1.8
Site A, 3.0 T	1.6	1.2	2.4	1.9
Site B, 3.0 T	2.3	1.9	3.1	2.5

reported in Table 4. Both T_1 and T_2 measurements in GM and WM were more reproducible at 3.0 T than 1.5 T according to their CVs (T_1-CVs = 6.6–7.6% at 1.5 T and 2.7–3.2% at 3.0 T; T_2-CVs = 9.7–14.0% at 1.5 T, and 8.5–10.4% at 3.0 T).

The results of the GLM analysis are reported in Fig. 8 and in Fig. 9. In Fig. 8 representative percentage bias values are reported for each tissue class. Based on GLM analysis, the test/retest associated bias was ≪1% for T_1 and <1% for T_2 measurements. In GM and WM, the T_1 bias caused by

Table 4
Inter-scanner coefficients-of-variation (CVs) for reproducibility of T1, T2, and self-normalized M0 (nM0) across grey matter, white matter, cerebrospinal fluid, and total volume. The CVs are reported for 1.5 T and 3.0 T.

T1-CV (%)	Grey matter	White matter	Cerebrospinal fluid	Total Volume
1.5 T	6.9	6.6	10.2	7.6
3.0 T	2.9	2.7	3.9	3.2
T2-CV (%)	Grey matter	White matter	Cerebrospinal fluid	Total Volume
1.5 T	14.0	9.7	20.5	13.3
3.0 T	10.4	8.5	15.2	10.5
nM0-CV (%)	Grey matter	White matter	Cerebrospinal fluid	Total Volume
1.5 T	5.1	4.2	6.9	5.2
3.0 T	4.5	4.0	6.0	4.7

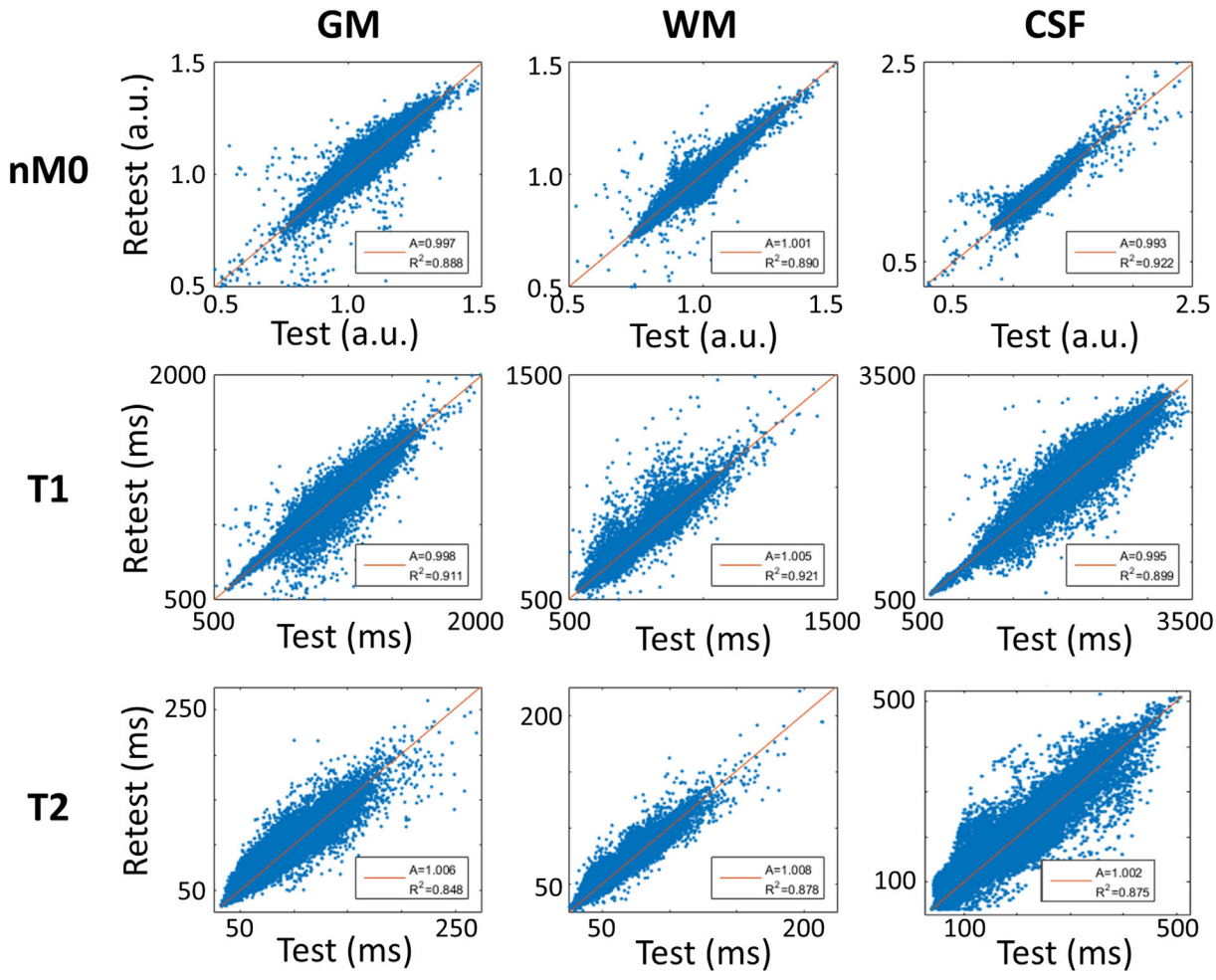

Fig. 7. Scatter plots of test/retest values of nM0, T1 and T2 for each subject at each system, sampling 1000 random points from GM, WM and CSF maps (45.000 points total). Each panel reports the slope of the linear fit (y = A*x) and the square of the Pearson's correlation coefficient (R^2).

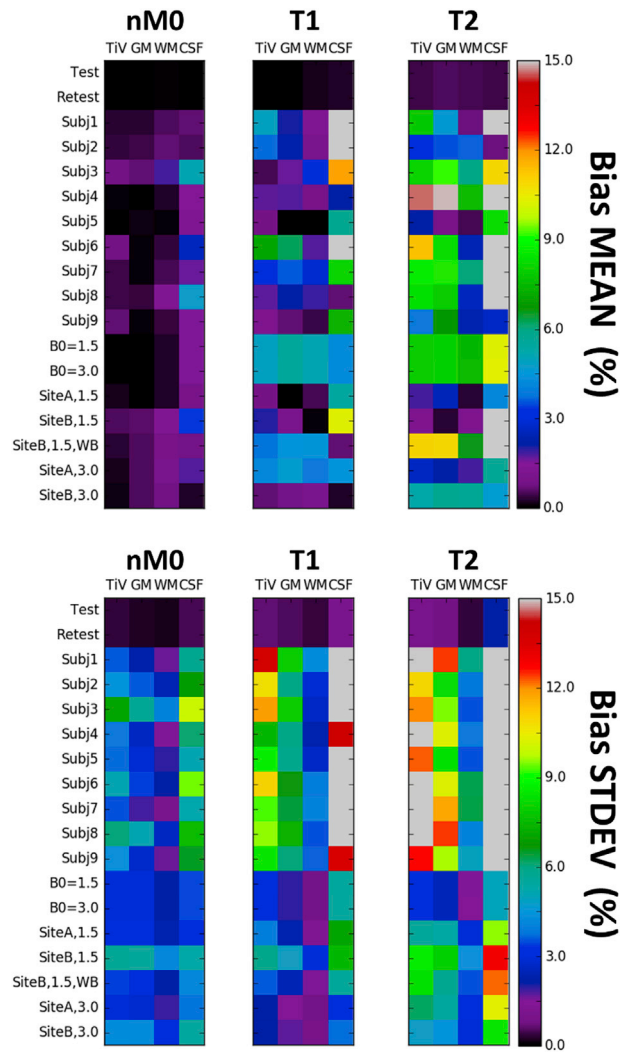

Fig. 8. The results of GLM analysis showing the bias values (beta) for each independent parameter, with betas normalized to the means of total volume grey matter (GM), white matter (WM), or cerebrospinal fluid (CSF) values for nM_0, T_1 and T_2. The values are reported in terms of ratio to the mean value, as that represents the variation caused by that variable. The T_1 variation caused by any parameter, including any single subject, is <5%. The T_2 values have the greatest variation from the 1.5 T wide-bore system (10%, outside CSF), while all other parameters account for <5% variation.

any parameter based on GLM analysis, including any single subject, was <10%. The T_2 values had the greatest bias when acquired in 1.5 T wide-bore system (11%), while other sites accounted for <5% variation. The effects of 1.5 T and 3.0 T fields on T_1 and T_2 (5–8%) were expected, due to their field dependencies.

In Fig. 9, local biases from the GLM analysis are reported in a central brain slice, to assess the local behaviour of the covariates in the model. It can be noted that nM_0 is variable between the center and the edges of the brain, with more variability between scanners operating at 3.0 T (β_{18} and β_{19}). While the average effect of field on nM0 was null due to the normalization process, T_1 values globally increased with field. T_1 effects did not display a significant spatial variation, but rather global effects. The values of T_2 globally decreased with field. The effect of site on T_2 did not display great spatial variation for the 1.5 T systems; however, the wide-bore system presented a global over-estimation across the brain. The 3.0 T sites displayed a spatial variability, from anterior to posterior.

Major variations in quantification of parameters were found for the 1.5 T wide-bore system at site B *in vivo*. In particular, with respect to the 1.5 T of site A, significant differences of T_1 and T_2 were found in GM and WM (p-values from 0.001 to 0.008), as well of nM_0 in CSF ($p = 0.03$). On the other hand, with respect to the 1.5 T of site B, the 1.5 T wide-bore scanner of site B presented significant differences of T_2 values in WM and CSF (p-values of 0.03 and 0.006 respectively), and of nM_0 in GM and WM ($p = 0.008$ and 0.02 respectively). Other significant differences were found between 3.0 T scanners for nM_0 values of GM and WM (both $p < 0.001$) and for T_1 values of GM ($p = 0.008$).

4. Discussion

This study performed MRF at five separate imaging systems, which included both 1.5 T and 3.0 T systems. We acquired SSFP MRF with the same sequence parameters and reconstruction methods at all sites. We assessed both repeatability and reproducibility of T_1 and T_2 measurements using the NIST/ISMRM phantom and in nine separate healthy volunteer brains scanned twice at all sites. We reported test/retest repeatability results using coefficients-of-variation averaged over tissue classes and assessed the performance of single voxels in scatter plots. General linear model analysis allowed reporting of local reproducibility biases, and coefficients-of-variations were also reported as a measure of reproducibility.

The phantom experiments showed a good agreement between intra- and inter-site T_1 and T_2 values. The phantom experiments were highly repeatable (CV<1%). Phantom reproducibility was high for T_1 values at 3.0 T (CV<0.2%) and at 1.5 T, which had a slightly higher CV (CV<0.9%). The phantom T_2 values were also more reproducible at 3.0 T than at 1.5 T according to their CVs (CV = 0.7% vs 2.7%), however limited conclusions should be drawn from this as the accuracy of our T_1 and T_2 values when compared to NIST values was highly dependent on the site. A limitation of our phantom study was the 5-degree temperature difference between Site A and Site B. We did not correct for temperature-related changes in the phantoms. Temperature differences were not present in human subjects due to thermoregulation. These MRF T_1 measurements had similar and better reproducibility to published multi-site inversion recovery (1.5 T RMS CV = 8.2%; 3.0 T RMS CV = 5.5%) and variable flip angle T_1 measurements (1.5 T RMS CV = 11.1%; 3.0 T CV = 22.9%), respectively, where the phantom temperature was tightly controlled (Bane et al., 2018). Our phantom experiments confirmed the repeatability of previous MRF literature, which showed less than 5% variation of T_1 and T_2 values measured with MRF over 34 consecutive days at 3.0 T, with similar higher variation in T_2 when compared with T_1 (Jiang et al., 2017b).

In addition to the phantom work, our study mainly focused on *in vivo* measurements in the human brain. The *in vivo* experiments were highly repeatable for T_1 measurements at all fields (CV<3.1%), while the CVs for T_2 measurements were slightly higher for 3.0 T (CV<7.8%) than 1.5 T (CV<7.0%), when excluding CSF. A spatial variability of nM_0 and T_2 was also seen in scanners operating at 3.0 T, with a spatial profile suggesting a difference due to B_{1+} fields. While higher field strengths have higher field non-uniformities that can affect repeatability, particularly from the faster signal dephasing of increased B_0 susceptibility and B_{1+} dielectric resonances (Vaughan et al., 1994) (Vaughan et al., 2001), our results demonstrated improved repeatability of T_1 at the higher field. These results suggest that T_1 measurements obtained with SSFP MRF are influenced less than T_2 by these non-uniformities, even without B_0 and B_{1+} inclusion in the dictionary. This may be related to the intrinsically lower SNR of 1.5 T over 3.0 T systems. However, T_2 had the opposite relationship than T_1 with field strength, as it was more repeatable and reproducible at the lower field strength according to GLM analysis.

Repeatability and reproducibility was higher for WM than for GM. This trend may be partly due to the topology of the two tissue classes, as GM voxels located at the interface between the other two tissues may include partial WM or CSF, due to imperfect segmentation and/or registration at the current resolution. Previous work has exploited the intrinsic multi-component nature of the MRF model by including partial volumes in the modelling (Hamilton et al., 2015). Including partial

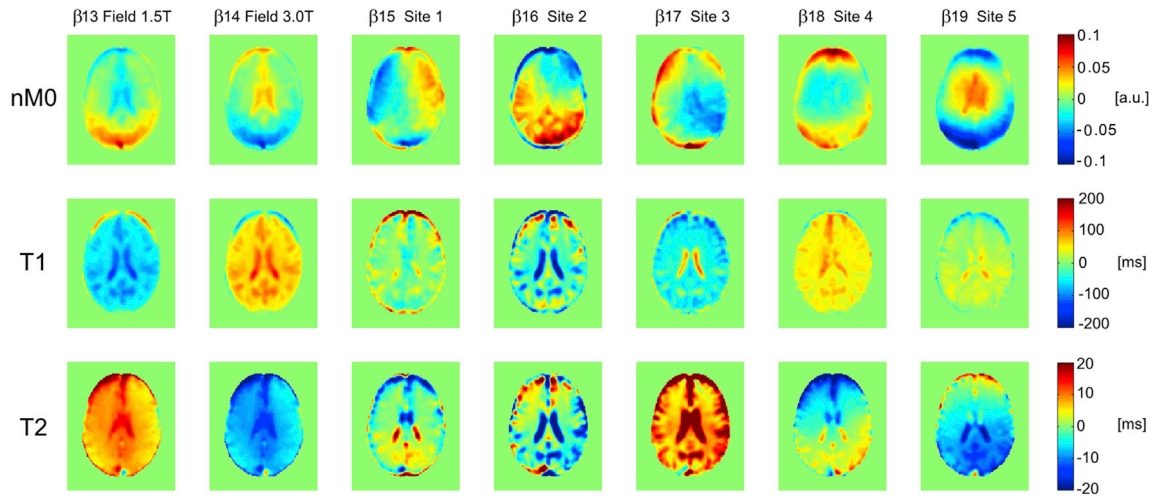

Fig. 9. Bias values (beta) estimated from the GLM analysis on a central brain slice, for nMo, T1 and T2 respectively. These values represent the local variation associated with the modeled effect (in this example field and site). As per the constraints in the model, the sum of the biases associated with the same effect is null ($\beta_{13} + \beta_{14} = 0$ and $\beta_{15} + \beta_{16} + \beta_{17} + \beta_{18} + \beta_{19} = 0$).

volume modelling in the simulations may further improve robustness of MRF at the expense of computation time and model complexity.

A relatively novel feature in this study was the analysis method used for estimating biases *in vivo*, using a GLM for separating the different covariates. Our analysis method builds on voxel-based morphometry (Wright et al., 1995), a fully-automated technique analyzing morphological differences between images of healthy or abnormal brains by performing voxel-wise statistical parametric maps (SPM) on segmented images (Ashburner and Friston, 2000). Here, rather than using pseudo-quantitative tissue probability maps, we used the estimated quantitative T_1 and T_2 maps within the analysis. This possibility has previously been applied to positron emission tomography (PET) (Ashburner), but has recently been used also for quantitative MRI data (Weiskopf et al., 2013) (Callaghan et al., 2014). It has been suggested that voxel-based methods, such as the one demonstrated here, can be used beyond repeatability studies in order to perform group analyses to identify disease and monitor treatment effects (Callaghan et al., 2014).

Importantly, our study was not limited to regions-of-interest, but estimated voxel-wise performance; variability was assessed using coefficients-of-variation, and bias using the GLM analysis. The GLM covariates having the lowest effect on bias were the variables of test and retest, with biases below 1% on average. This is unsurprising as there should be no mean bias between test and retest. Field strength introduced the highest bias for T_1 and T_2 measurements. Following field, the highest T_1 bias was introduced by the site differences, while T_2 was affected mostly by subject bias. Our local assessment of site-related variabilities showed the greatest spatial distribution of bias in nM_0, followed by T_2 (Fig. 9). The nM_0 variations were mostly between the center and the edges of the brain, which may be explained by the different system receiver arrays and the subjects being positioned in slightly different locations within the arrays, since each array would have different sensitivity profiles. As M_0 is estimated as a scaling factor of the received signal, all local variations in the receiver profile result in a multiplicative factor to M_0. On the other hand, T_2 local variation was higher at 3.0 T and had a smooth gradient from anterior to posterior. This could be potentially explained by positioning or local variations of the transmitted B_1+ field and by increased dielectric resonance (B_{1+}) (Kangarlu et al., 1999). As T_2 estimation relies on a precise flip angle in order to obtain stimulated echoes, it is known that B_1+ can affect its accuracy (Buonincontri and Sawiak, 2016).

Repeatability and reproducibility values measured here for 2D MRF were also in line with Körzdörfer et al. (2018), which used a different study protocol and custom ROI analysis but a similar pulse sequence. The quantitative T_1 and T_2 parameters obtained in the brain from our MRF study were within the wide range of those obtained in previous non-MRF studies for healthy volunteers, using different relaxometry methods (McPhee and Wilman, 2017) (Whittall et al., 1997) (Jiang et al., 2015) (Stikov et al., 2015). Landman et al. (2011) assessed repeatability of several sequences, including quantitative T_1 and T_2 in the brain, measured with variable flip angle and multi-echo spin echo respectively, reporting CVs in GM and WM of up to 4% for T_1 and 20% for T_2 (Landman et al., 2011). Bauer et al. (2010) reported reproducibility of dual echo fast spin-echo on three different scanners, showing variability up to 20% (Bauer et al., 2010). Deoni et al. (2008) performed a multi-center study including three different scanners at 1.5T assessing driven equilibrium single pulse observation (DESPOT) of T_1 and T_2, and reported *in vivo* reproducibility CV values of 6.5% for T_1 and 8% for T_2 respectively (Deoni et al., 2008). Although CVs cannot be directly compared across studies due to the variations in protocols and analyses, 2D MRF precision is promising in the context of similar studies in the literature. While these studies have assessed repeatability and reproducibility, these values will change under different resolutions, flip angle/TR lists, and simulation parameters. These measurements can be considered a baseline for comparison with future MRF brain measurements that attempt to increase resolution or temporal efficiency.

An important feature of the MRF technique is the high temporal efficiency. For instance, the acquisition here, based on (Jiang et al., 2015), took just over 10 s to acquire each slice. Despite the short acquisition times, we saw highly-repeatable quantification, especially for T_1 estimates. In fact, similar MRF implementations are achieving highly-discriminatory biomarkers for brain cancer (Badve et al., 2016), epilepsy (Liao et al., 2018), abdominal cancer (Chen et al., 2016) and prostate cancer (Yu et al., 2017), with the promise of contributing significantly to diagnosis. Our results confirm that MRF is reliable as a fast T_1 and T_2 measurement technique, hence encouraging more evaluation. Further studies are also required to compare reliability of T_1 and T_2 maps with MRF with other emerging quantitative techniques.

The MRF SSFP acquisition used here performed much better on GM and WM than CSF. One reason for this is the low SNR of CSF, due to the relatively high flip-angles used in the MRF pulse schedule, needed to achieve stimulated echoes. Secondly, the dictionary is built with different sampling densities depending on T_1 and T_2, and the sparser dictionary values for the look-up table in the ranges of CSF values may contribute to the high variability. Lastly, the higher variability of parameters in CSF may be due to the effects of diffusion introduced by the spoiler gradients (Jiang et al., 2015). Here, the gradients used were designed to dephase a

2 mm slice by 8π, which is more than twice that reported in the original SSFP MRF paper (Jiang et al., 2015), where 5 mm slices were used with the same amount of dephasing. It has been previously shown that the spoilers at the end of each TR in SSFP MRF generate diffusion sensitivity (Kobayashi and Terada, 2018), and that it is possible to exploit this effect in order to estimate diffusion parameters in MRF (Jiang et al., 2017a). However, despite the promise of adding more relevant estimations and obtain more robust T_1 and T_2 estimates, the performance of SSFP estimations including diffusion is known to be limited by dictionary size and physiological motion occurring throughout the acquisitions (Jiang et al., 2017a).

To be able to better compare our results to others, here we have used the acquisition described in Jiang et al. (2015) (Jiang et al., 2015), which has been one of the most widely used MRF methods in literature so far. As this work confirmed, this acquisition scheme has low sensitivity to off-resonance values, which enables estimates of T_1 and T_2 accurately without including more parameters in the model. The inclusion of further parameters to the dictionary may also improve MRF repeatability. For instance, it is known that including B_{1+} effects in the SSFP MRF estimates improves accuracy of T_2 values (Buonincontri and Sawiak, 2016) (Ma et al., 2017), hence it is very likely that this would improve the repeatability of MRF. However, the inclusion of B_1+ in the schedule used by Jiang et al., 2015 leads to errors in the estimates (Buonincontri and Sawiak, 2016), and modifications are needed such as RF spoiling (Cloos et al., 2016) or abrupt changes in flip angle (Buonincontri and Sawiak, 2016). Local effects of receiver coil B_{1-} are mostly superimposed to the nM_0 maps, however as M_0 is estimated as a scaling factor to the signal evolutions and not fully-modeled, receiver effects are difficult to include in the model.

One of the strengths of this study was that the gradient trajectory and reconstruction was identical for all acquired data. We used the same k-space acquisition trajectories with the center of the brain near the scanners' isocenters throughout this study, but did not investigate the effects of concomitant gradient fields, which could create signal dephasing when imaging far from isocenter (King et al., 1999) (Hofstetter et al., 2017). Also, here we did not perform a full trajectory measurement but based our trajectory corrections on a single gradient delay for each scanner. In our data, the available range of head positions and rotations was limited, which would increase our repeatability by reducing the effects of blood pooling or diffusion.

One of the limitations of our study was the relatively small number of healthy subjects included ($n = 9$). In order to extend these results to the general population and to disease diagnosis and treatment assessment, repeatability and reproducibility could be assessed also in larger populations with studies that include multiple pathologies. Although pathological studies are ideal for quantifying reproducibility, such a study is difficult in practice where the study would introduce additional stress on the patient. Healthy volunteer reproducibility studies are important as an initial indicator of whether a patient study will be successful.

While this is a confirmation of test/retest repeatability and reproducibility, further confirmations could be done across multiple systems and vendors to validate the use of MRF for longitudinal imaging or multisite studies. This study demonstrated reproducibility within brain imaging; similar experiments could be repeated in other anatomical regions. The MRF experiments in the body could be complicated by the presence of fat and less homogeneous magnetic fields. However, new approaches including fat fraction as well as B_0 and/or B_{1+} in the signal model are promising solutions (Cloos et al., 2016).

5. Conclusion

We have reported the assessment of the test/retest repeatability and of the reproducibility of physical parameter measures when using MRF in the healthy human brain at 1.5 T and 3.0 T. Test/retest Magnetic resonance fingerprinting was able to achieve an excellent repeatability and a good reproducibility in a short scan time. Accurate and reproducible signals are key in discriminating longitudinal changes due to disease and treatment, and these repeatability and reproducibility results encourage further investigations of MR Fingerprinting for clinical applications.

Acknowledgements

Funding: this work was supported by Cancer Research UK, INFN CSN5, from the European Commission (Grant Agreement Number 656937), and from the Royal Society (IE150411). JK acknowledges support by GlaxoSmithKline. FAG, FR and FZ receive support from the Engineering and Physical Sciences Research Council (C197/A16465) and Cancer Research UK (C19212/A29082, C19212/A27150). The project was also supported by the Addenbrooke's Charitable Trust (ACT) and the National Institute of Health Research (NIHR) Cambridge Biomedical Research Centre (BRC) award to Cambridge University Hospitals (CUH) NHS Foundation Trust in partnership with the University of Cambridge.

Appendix A. Supplementary data

Supplementary data related to this article can be found at https://doi.org/10.1016/j.neuroimage.2019.03.047.

References

Ashburner, J., 2012. SPM: a history. Neuroimage 62, 791–800.
Ashburner, J., Friston, K.J., 2000. Voxel-based morphometry–the methods. Neuroimage 11, 805–821.
Badve, C., Yu, A., Dastmalchian, S., Rogers, M., Ma, D., Jiang, Y., Margevicius, S., Pahwa, S., Lu, Z., Schluchter, M., 2016. MR fingerprinting of adult brain tumors: initial experience. Am. J. Neuroradiol. 38, 492–499.
Bane, O., Hectors, S.J., Wagner, M., Arlinghaus, L.L., Aryal, M.P., Cao, Y., Chenevert, T.L., Fennessy, F., Huang, W., Hylton, N.M., 2018. Accuracy, repeatability, and interplatform reproducibility of T1 quantification methods used for DCE-MRI: results from a multicenter phantom study. Magn. Reson. Med. 79, 2564–2575.
Bartzokis, G., Sultzer, D., Cummings, J., Holt, L.E., Hance, D.B., Henderson, V.W., Mintz, J., 2000. In vivo evaluation of brain iron in Alzheimer disease using magnetic resonance imaging. Arch. Gen. Psychiatr. 57, 47–53.
Baudrexel, S., Nürnberger, L., Rüb, U., Seifried, C., Klein, J.C., Deller, T., Steinmetz, H., Deichmann, R., Hilker, R., 2010. Quantitative mapping of T1 and T2* discloses nigral and brainstem pathology in early Parkinson's disease. Neuroimage 51, 512–520.
Bauer, C.M., Jara, H., Killiany, R., Initiative, A.s.D.N., 2010. Whole brain quantitative T2 MRI across multiple scanners with dual echo FSE: applications to AD, MCI, and normal aging. Neuroimage 52, 508–514.
Beckmann, C.F., Jenkinson, M., Smith, S.M., 2003. General multilevel linear modeling for group analysis in FMRI. Neuroimage 20, 1052–1063.
Begley, C.G., Ellis, L.M., 2012. Drug development: raise standards for preclinical cancer research. Nature 483, 531–533.
Bernhardt, B.C., Fadaie, F., de Wael, R.V., Hong, S.-J., Liu, M., Guiot, M.C., Rudko, D.A., Bernasconi, A., Bernasconi, N., 2018. Preferential susceptibility of limbic cortices to microstructural damage in temporal lobe epilepsy: a quantitative T1 mapping study. Neuroimage 294–303.
Bland, J.M., Altman, D.G., 1999. Measuring agreement in method comparison studies. Stat. Methods Med. Res. 8, 135–160.
Buonincontri, G., Sawiak, S.J., 2016. MR fingerprinting with simultaneous B1 estimation. Magn. Reson. Med. 76, 1127–1135.
Callaghan, M.F., Freund, P., Draganski, B., Anderson, E., Cappelletti, M., Chowdhury, R., Diedrichsen, J., FitzGerald, T.H., Smittenaar, P., Helms, G., 2014. Widespread age-related differences in the human brain microstructure revealed by quantitative magnetic resonance imaging. Neurobiol. Aging 35, 1862–1872.
Chen, Y., Jiang, Y., Pahwa, S., Ma, D., Lu, L., Twieg, M.D., Wright, K.L., Seiberlich, N., Griswold, M.A., Gulani, V., 2016. MR fingerprinting for rapid quantitative abdominal imaging. Radiology 279, 278–286.
Cloos, M.A., Knoll, F., Zhao, T., Block, K.T., Bruno, M., Wiggins, G.C., Sodickson, D.K., 2016. Multiparametric imaging with heterogeneous radiofrequency fields. Nat. Commun. 7, 12445.
Deoni, S.C., 2010. Quantitative relaxometry of the brain. Top. Magn. Reson. Imag.: TMRI 21, 101.
Deoni, S.C., Williams, S.C., Jezzard, P., Suckling, J., Murphy, D.G., Jones, D.K., 2008. Standardized structural magnetic resonance imaging in multicentre studies using quantitative T1 and T2 imaging at 1.5 T. Neuroimage 40, 662–671.
Friedman, S., Shaw, D., Artru, A., Richards, T., Gardner, J., Dawson, G., Posse, S., Dager, S., 2003. Regional brain chemical alterations in young children with autism spectrum disorder. Neurology 60, 100–107.
Friston, K.J., Holmes, A.P., Worsley, K.J., Poline, J.P., Frith, C.D., Frackowiak, R.S., 1994. Statistical parametric maps in functional imaging: a general linear approach. Hum. Brain Mapp. 2, 189–210.
Goto, M., Abe, O., Aoki, S., Hayashi, N., Miyati, T., Takao, H., Iwatsubo, T., Yamashita, F., Matsuda, H., Mori, H., 2013. Diffeomorphic Anatomical Registration through

Exponentiated Lie Algebra provides reduced effect of scanner for cortex volumetry with atlas-based method in healthy subjects. Neuroradiology 55, 869–875.
Gracien, R.M., Reitz, S.C., Hof, S.M., Fleischer, V., Droby, A., Wahl, M., Steinmetz, H., Groppa, S., Deichmann, R., Klein, J.C., 2017. Longitudinal quantitative MRI assessment of cortical damage in multiple sclerosis: a pilot study. J. Magn. Reson. Imaging 46, 1485–1490.
Hamilton, J.I., Griswold, M.A., Seiberlich, N., 2015. MR Fingerprinting with chemical exchange (MRF-X) to quantify subvoxel T1 and extracellular volume fraction. J. Cardiovasc. Magn. Reson. 17, W35.
Hendry, J., DeVito, T., Gelman, N., Densmore, M., Rajakumar, N., Pavlosky, W., Williamson, P.C., Thompson, P.M., Drost, D.J., Nicolson, R., 2006. White matter abnormalities in autism detected through transverse relaxation time imaging. Neuroimage 29, 1049–1057.
Hofstetter, L.W., Morrell, G., Kaggie, J., Kim, D., Carlston, K., Lee, V.S., 2017. T2* Measurement bias due to concomitant gradient fields. Magn. Reson. Med. 77, 1562–1572.
Jackson, J.I., Meyer, C.H., Nishimura, D.G., Macovski, A., 1991. Selection of a convolution function for Fourier inversion using gridding [computerised tomography application]. Medical Imaging, IEEE Transactions on 10, 473–478.
Jiang, Y., Hamilton, J., Lo, W.-C., Wright, K., Ma, D., Coristine, A., Seiberlich, N., Gulani, V., Griswold, M., 2017a. Simultaneous T1, T2 and diffusion quantification using multiple contrast prepared magnetic resonance fingerprinting. Proc Intl Soc Magn Reson Med 25, 1171.
Jiang, Y., Ma, D., Keenan, K.E., Stupic, K.F., Gulani, V., Griswold, M.A., 2017b. Repeatability of magnetic resonance fingerprinting T1 and T2 estimates assessed using the ISMRM/NIST MRI system phantom. Magn. Reson. Med. 78, 1452–1457.
Jiang, Y., Ma, D., Seiberlich, N., Gulani, V., Griswold, M.A., 2015. MR fingerprinting using fast imaging with steady state precession (FISP) with spiral readout. Magn. Reson. Med. 74, 1621–1631.
Kaggie, J., Buonincontri, G., Biagi, L., Retico, A., McLean, M., Riemer, F., Schulte, R., Gomez, P., Graves, M., Tosetti, M., Gallagher, F.A., 2019. MR Fingerprinting Repeatability in the Brain Dataset. https://doi.org/10.17863/CAM.37467.
Kangarlu, A., Baertlein, B.A., Lee, R., Ibrahim, T., Yang, L., Abduljalil, A.M., Robitaille, P.-M.L., 1999. Dielectric resonance phenomena in ultra high field MRI. J. Comput. Assist. Tomogr. 23, 821–831.
King, K.F., Ganin, A., Zhou, X.J., Bernstein, M.A., 1999. Concomitant gradient field effects in spiral scans. Magn. Reson. Med. 41, 103–112.
Kobayashi, Y., Terada, Y., 2018. Diffusion-weighting caused by spoiler gradients in the fast imaging with steady-state precession sequence may lead to inaccurate T2 measurements in MR fingerprinting. Magnetic Resonance in Medical Sciences tn. 2018-0027.
Körzdörfer, G., Kirsch, R., Liu, K., Pfeuffer, J., Hensel, B., Jiang, Y., Ma, D., Griswold, M., Gulani, V., Nittka, M., 2018. Multicenter and multiscanner reproducibility of Magnetic Resonance Fingerprinting relaxometry in the brain. Proc Intl Soc Mag Reson Med 0798.
Landman, B.A., Huang, A.J., Gifford, A., Vikram, D.S., Lim, I.A.L., Farrell, J.A., Bogovic, J.A., Hua, J., Chen, M., Jarso, S., 2011. Multi-parametric neuroimaging reproducibility: a 3-T resource study. Neuroimage 54, 2854–2866.
Larsson, H., Frederiksen, J., Petersen, J., Nordenbo, A., Zeeberg, I., Henriksen, O., Olesen, J., 1989. Assessment of demyelination, edema, and gliosis by in vivo determination of T1 and T2 in the brain of patients with acute attack of multiple sclerosis. Magn. Reson. Med. 11, 337–348.
Lawrence, I., Lin, K., 1989. A concordance correlation coefficient to evaluate reproducibility. Biometrics 255–268.
Liao, C., Wang, K., Cao, X., Li, Y., Wu, D., Ye, H., Ding, Q., He, H., Zhong, J., 2018. Detection of lesions in mesial temporal lobe epilepsy by using MR fingerprinting. Radiology 172131.
Ma, D., Coppo, S., Chen, Y., McGivney, D.F., Jiang, Y., Pahwa, S., Gulani, V., Griswold, M.A., 2017. Slice profile and B1 corrections in 2D magnetic resonance fingerprinting. Magn. Reson. Med. 78, 1781–1789.
Ma, D., Gulani, V., Seiberlich, N., Liu, K., Sunshine, J.L., Duerk, J.L., Griswold, M.A., 2013. Magnetic resonance fingerprinting. Nature 495, 187–192.
Majumdar, S., Orphanoudakis, S., Gmitro, A., O'donnell, M., Gore, J., 1986. Errors in the measurements of T2 using multiple-echo MRI techniques. II. Effects of static field inhomogeneity. Magn. Reson. Med. 3, 562–574.
Mann, H.B., Whitney, D.R., 1947. On a test of whether one of two random variables is stochastically larger than the other. Ann. Math. Stat. 50–60.
McBride, G., 2005. A Proposal For Strength-of-Agreement Criteria For Lin's Concordance Correlation Coefficient. NIWA Client Report: HAM2005-062.
McPhee, K.C., Wilman, A.H., 2017. Transverse relaxation and flip angle mapping: evaluation of simultaneous and independent methods using multiple spin echoes. Magn. Reson. Med. 77, 2057–2065.
Nelson, T., Tung, S., 1987. Temperature dependence of proton relaxation times in vitro. Magn. Reson. Imag. 5, 189–199.
Penny, W.D., Friston, K.J., Ashburner, J.T., Kiebel, S.J., Nichols, T.E., 2011. Statistical Parametric Mapping: the Analysis of Functional Brain Images. Elsevier.
Pitkanen, A., Laakso, M., Kalviainen, R., Partanen, K., Vainio, P., Lehtovirta, M., Riekkinen, P., Soininen, H., 1996. Severity of hippocampal atrophy correlates with the prolongation of MRI T sub 2 relaxation time in temporal lobe epilepsy but not in Alzheimer's disease. Neurology 46, 1724–1730.
Sbrizzi, A., van der Heide, O., Cloos, M., van der Toorn, A., Hoogduin, H., Luijten, P.R., van den Berg, C.A., 2018. Fast quantitative MRI as a nonlinear tomography problem. Magn. Reson. Imag. 46, 56–63.
Stikov, N., Boudreau, M., Levesque, I.R., Tardif, C.L., Barral, J.K., Pike, G.B., 2015. On the accuracy of T1 mapping: searching for common ground. Magn. Reson. Med. 73, 514–522.
Sung, K., Daniel, B.L., Hargreaves, B.A., 2013. Transmit field inhomogeneity and T1 estimation errors in breast DCE-MRI at 3 tesla. J. Magn. Reson. Imaging 38, 454–459.
Tanenbaum, L.N., Tsiouris, A.J., Johnson, A.N., Naidich, T.P., DeLano, M.C., Melhem, E.R., Quarterman, P., Parameswaran, S., Shankaranarayanan, A., Goyen, M., 2017. Synthetic MRI for clinical neuroimaging: results of the magnetic resonance image compilation (MAGiC) prospective, multicenter, multireader trial. Am. J. Neuroradiol. 38, 1103–1110.
Tang, X., Cai, F., Ding, D.-X., Zhang, L.-L., Cai, X.-Y., Fang, Q., 2018. Magnetic resonance imaging relaxation time in Alzheimer's disease. Brain Res. Bull. 140, 176–189. https://doi.org/10.1016/j.brainresbull.2018.05.004.
Tofts, P., 2005. Quantitative MRI of the Brain: Measuring Changes Caused by Disease. John Wiley & Sons.
Vaughan, J.T., Garwood, M., Collins, C.M., Liu, W., DelaBarre, L., Adriany, G., Andersen, P., Merkle, H., Goebel, R., Smith, M.B., Ugurbil, K., 2001. 7T vs. 4T: RF power, homogeneity, and signal-to-noise comparison in head images. Magn. Reson. Med. 46, 24–30.
Vaughan, J.T., Hetherington, H.P., Otu, J.O., Pan, J.W., Pohost, G.M., 1994. High frequency volume coils for clinical NMR imaging and spectroscopy. Magn. Reson. Med. 32, 206–218.
Vymazal, J., Righini, A., Brooks, R.A., Canesi, M., Mariani, C., Leonardi, M., Pezzoli, G., 1999. T1 and T2 in the brain of healthy subjects, patients with Parkinson disease, and patients with multiple system atrophy: relation to iron content. Radiology 211, 489–495.
Walsh, D.O., Gmitro, A.F., Marcellin, M.W., 2000. Adaptive reconstruction of phased array MR imagery. Magn. Reson. Med. 43, 682–690.
Weiskopf, N., Suckling, J., Williams, G., Correia, M.M., Inkster, B., Tait, R., Ooi, C., Bullmore, E.T., Lutti, A., 2013. Quantitative multi-parameter mapping of R1, PD*, MT, and R2* at 3T: a multi-center validation. Front. Neurosci. 7, 95.
Whittall, K.P., Mackay, A.L., Graeb, D.A., Nugent, R.A., Li, D.K., Paty, D.W., 1997. In vivo measurement of T2 distributions and water contents in normal human brain. Magn. Reson. Med. 37, 34–43.
Wiesinger, F., Janich, M., Ljungberg, E., Barker, G., Solana, A.B., 2018. 3D MR parameter mapping using magnetization prepared zero TE. Proc Intl Soc Mag Reson Med 0061.
Williamson, P., Pelz, D., 1992. Frontal, temporal, and striatal proton relaxation times in schizophrenic patients and normal comparison subjects. Am. J. Psychiatry 149, 549.
Wright, I.C., McGuire, P.K., Poline, J.B., Travere, J.M., Murray, R.M., Frith, C.D., Frackowiak, R.S., Friston, K.J., 1995. A voxel-based method for the statistical analysis of gray and white matter density applied to schizophrenia. Neuroimage 2, 244–252.
Yankeelov, T.E., Pickens, D.R., Price, R.R., 2011. Quantitative MRI in Cancer. Taylor & Francis.
Yu, A.C., Badve, C., Ponsky, L.E., Pahwa, S., Dastmalchian, S., Rogers, M., Jiang, Y., Margevicius, S., Schluchter, M., Tabayoyong, W., 2017. Development of a combined MR fingerprinting and diffusion examination for prostate cancer. Radiology 283, 729–738.